Available online at www.sciencedirect.com
SCIENCE DIRECT®
Journal of Computational Physics 212 (2006) 318–337
JOURNAL OF COMPUTATIONAL PHYSICS
www.elsevier.com/locate/jcp

High velocity impact of metal sphere on thin metallic plates: A comparative smooth particle hydrodynamics study

Vishal Mehra *, Shashank Chaturvedi

Institute for Plasma Research, Pulse Power, Near Indira Bridge, Bhat, Gandhinagar 382 428, Gujarat, India

Received 20 October 2004; received in revised form 27 April 2005; accepted 29 June 2005
Available online 15 August 2005

Abstract

Four different shock-capturing schemes used in smooth particle hydrodynamics are compared as applied to moderately high-velocity impacts (at 3 km/s) and hypervelocity impacts (at ~6 km/s) of metallic projectiles on thin metal plates. The target and projectile may be of same metal or different. The simulations are compared with previously published experimental data and simulations. The schemes differ in how artificial viscosity (AV) is treated and include (i) standard SPH AV, (ii) Balsara's AV (BAL), (iii) Morris and Monaghan's AV (MON) and (iv) Riemann-based contact algorithm (CON) of Parshikov et al. At moderately high impact velocity, CON performed best overall, in particular, in being free from numerical fracture and formation of clumps, problems that plague SAV and its modifications, BAL and MON. For the hypervelocity impact, CON does not produce correct debris cloud. The BAL and MON while reproducing the debris cloud more closely, overestimate the crater diameter significantly. An excessive AV, by enhancing transverse momentum flow, may be the source of the overestimation of crater diameter. Experimental agreement is generally worse when the target and projectile are formed of distinct metals.

Keywords: Hypervelocity impact; Artificial viscosity; Riemann problem; Hydrocode

1. Introduction

Smooth particle hydrodynamics (SPH) is a non-grid based computational technique meant for continuum dynamics simulations. As such, it competes with conventional grid-based Eulerian and Lagrangian techniques. However, SPH is most often applied to astrophysical problems [1,2] and problems involving large material deformation, e.g., high-speed impact of solid bodies [3], chemical explosions [4] and explosive

* Corresponding author.
E-mail address: vmehra@ipr.res.in (V. Mehra).

0021-9991/$ - see front matter © 2005 Published by Elsevier Inc.
doi:10.1016/j.jcp.2005.06.020

forming in industry [5], etc. During large deformations, conventional grid-based techniques have trouble with grid entanglement, and require complex regridding procedures to deal with the problem. SPH, being grid-less and employing pseudo-particles, does not face this particular problem. In SPH, the continuum fields such as velocities, pressure, local density, temperature and stresses are carried by a set of moving, interacting (pseudo) particles; and the inter-particle interactions are derived from the continuum equations through interpolation and discretization.

SPH has been proposed and implemented in several formulations e.g. [6–11]. One way these formulations differ among themselves is in how they tackle the problem of *shock-capturing*. The problem is that real shocks are very thin discontinuities in the solution and hence are computationally expensive to obtain and propagate. The most common way to capture shocks has been to use artificial viscosity (AV) in the standard SPH form (SAV) [2]. However, SAV tends to overestimate the viscosity, and modifications have been proposed of which the most popular are Balsara's (BAL) [12] and Morris and Monaghan's (MON) [13] forms. Another SPH formulation dispenses with AV altogether and instead achieves shock-capturing through the so-called Riemann solver [14]. Riemann techniques are widely applied in modern mesh-based techniques but have seen only limited use in SPH [15,16]. A recent implementation of the Riemann technique within SPH is referred to as contact SPH (CON) [17,18].

The interaction between SPH particles is through the kernel function W. The kernel W depends upon the inter-particle separation $|x - \acute{x}|$ and a parameter h called the *smoothing length*. The kernel W must satisfy certain basic conditions:

(i) W must reduce to a delta function in the limit of small smoothing length

$$\lim_{h\to 0} W(x-\acute{x},h) = \delta(x-\acute{x}). \tag{1}$$

(ii) W must be normalized

$$\int W(x,h)\,\mathrm{d}x = 1. \tag{2}$$

(iii) W must have compact support

$$W(x,h) = 0 \quad \text{for } |x| \geqslant R \text{ for some } R > 0. \tag{3}$$

Employment of a kernel function transforms the partial differential equations of continuum dynamics into integral equations through the *kernel estimate*

$$\langle f(x)\rangle = \int f(\acute{x})W(x-\acute{x},h)\,\mathrm{d}\acute{x}. \tag{4}$$

The integral is discretized to a sum over particles, i.e.,

$$\langle f(x_i)\rangle \approx \sum_{j=1}^{N} m_j f_j W(x_i - x_j, h)/\rho_j. \tag{5}$$

Here, m_j is the mass and ρ_j is the density associated with the jth particle, and $f_j = f(x)_{x=x_j}$. Integrating the above equation by parts and using the compactness property of W, we get an expression for the derivative

$$\langle \nabla f(x)\rangle_{x=x_i} \approx -\sum_{j=1}^{N} m_j f_j \nabla_j W(x_i - x_j, h)_{x=x_j}/\rho_j. \tag{6}$$

These equations yield estimates for accelerations, strain rates and so on.

Now, the basic equations of continuum mechanics, expressing conservation of mass, momentum and energy, are given by

$$\begin{aligned}\frac{\mathrm{d}\rho}{\mathrm{d}t} &= -\rho\nabla\cdot\mathbf{v},\\ \frac{\mathrm{d}\mathbf{v}}{\mathrm{d}t} &= \frac{1}{\rho}\nabla\cdot\sigma,\\ \frac{\mathrm{d}E}{\mathrm{d}t} &= \frac{1}{\rho}\sigma\cdot\nabla\mathbf{v},\end{aligned} \tag{7}$$

where $\mathrm{d}/\mathrm{d}t$ refers to the convective derivative, ρ is the density, E is the internal energy per unit mass, and σ is the stress tensor.

Combining these equations with the estimates for accelerations, etc., we get the set of discretized equations

$$\begin{aligned}\frac{\mathrm{d}\rho_i}{\mathrm{d}t} &= \rho_i\sum_j\frac{m_j}{\rho_j}(\mathbf{v_i}-\mathbf{v_j})\cdot\nabla W_{ij},\\ \frac{\mathrm{d}\mathbf{v}_i}{\mathrm{d}t} &= -\sum_j m_j\left(\frac{\sigma_i}{\rho_i^2}+\frac{\sigma_j}{\rho_j^2}+\Pi_{ij}\mathbf{I}\right)\cdot\nabla W_{ij},\\ \frac{\mathrm{d}E_i}{\mathrm{d}t} &= -\sum_j m_j(\mathbf{v_i}-\mathbf{v_j})\cdot\left(\frac{\sigma_i}{\rho_i^2}+\frac{1}{2}\Pi_{ij}\mathbf{I}\right)\cdot\nabla W_{ij}.\end{aligned} \tag{8}$$

Π_{ij} is an artificial viscous pressure discussed below. It is required to control unphysical oscillations around shocks. The summations run over neighboring particles. We also have

$$\begin{aligned}W_{ij} &= W(|x_i-x_j|/h),\\ \nabla W_{ij} &= \nabla W(|x_i-x_j|/h)|_{x=x_j}.\end{aligned}$$

Several kernel functions have been used in SPH. A comparative analysis of 10 different kernels has been reported [22], advocating the use of a quintic spline kernel. However, the quintic spline has larger support and thus would have a larger number of neighbors which need to be summed over. In our code, we implement the more widely used cubic B-spline, which offers a compromise between accuracy and computational efficiency

$$W = \begin{cases}\frac{C}{h^D}\left[1-\frac{3}{2}z^2+\frac{3}{4}z^3\right], & z<1,\\ \frac{C}{4h^D}[2-z]^3, & 1\leqslant z<2,\\ 0, & z\geqslant 2,\end{cases} \tag{9}$$

where $z=|x_i-x_j|/h$, D is the spatial dimension of the problem ((1), (2) or (3)). C is a dimension-dependent normalization factor, being $(2/3)$, $10/7\pi$ and $1/\pi$ for $D=1,2$ and 3, respectively.

The existence of numerous competing SPH formulations may well confuse a beginner, since few studies exist that compare different formulations [19,20]. In addition, artificial viscosity prescriptions, except for the Riemann methods, generally contain parameters whose values are only fixed empirically. Another parameter, obligatory to SPH schemes, is h/d, the ratio between the smoothing length h and inter-particle distance d. In general, the smoothing lengths are allowed to vary in space and time and h/d is defined as the ratio between the *initial* inter-particle separation and the *initial* local smoothing length. Generally speaking, h/d is not a local quantity: all the inter-particle separations are uniformly scaled to yield smoothing lengths. A good SPH technique should be robust against small changes in h/d. The parameter h/d may not take arbitrary values and is generally set to values between 1 and 2. The theoretical justification for this choice

is largely lacking, except for an analysis of one-dimensional SPH carried out by Balsara [12], that showed that arbitrary values of h/d give erroneous results and the simulations must be run in a narrower band of *good* h/d values. Balsara provided values for good ranges of the h/d parameter in the case of particular kernel functions, viz., third and fourth order splines. However, Balsara's analysis was applied only to strengthless situations.

In this study, we compare four different SPH methods: SAV, BAL, MON and CON (detailed below), as applied to high-velocity impact of metal spheres on thin metallic plates. We examine the cases with identical as well as different metals in the impactor and target. For the parameter ranges examined, the plates are completely penetrated and a debris cloud is formed behind the plate, consisting of both projectile and target material. The passage of the projectile through the target also leads to the formation of a crater in the target plate.

We compare our simulation results for three parameters, viz., the crater diameter, the aspect ratio of the debris cloud and the pressure/tension produced at specified locations, with previously published experimental or simulation results. These comparisons are made at specified times. The simulations are repeated at different h/d values for each AV method to check the robustness of the results and to obtain good ranges for h/d.

Two different impact situations are considered in this paper. The first is the impact at 3.1 km/s of 1 cm diameter steel and aluminium (Al) spheres onto a 0.2 cm thick aluminium plate. These simulations are done in planar geometry and make use of an elastic–perfectly plastic constitutive model in order to permit a comparison with the simulations of Howell and Ball [21]. The second is the impact of 1 cm diameter aluminium (Al) spheres onto Al and copper (Cu) plates at 6.18 and 5.75 km/s, respectively. These simulations are compared with the experiments of [23], are done in both two and three dimensions, and use more realistic equations of state and strength models.

This paper is organized as follows. In Section 2, we describe the various artificial viscosity schemes that have been used in this paper. Section 3 describes the simulations in detail along with their results. Section 4 contains a discussion and conclusions.

2. Artificial viscosities

Four different SPH schemes are compared here, the first being the standard SPH artificial viscosity (SAV). The AV terms are added to the momentum equation and consist of two contributions: one linear and the other quadratic in the divergence of velocity, analogous to the von Neumann–Richtmeyer AV used in mesh-based codes. The AV pressure Π_{ij}, which produces a force on the particle i due to the presence of particle j, is given by

$$\Pi_{ij} = \begin{cases} \frac{-\alpha c_{ij}(\mu_{ij} - \frac{\beta}{2}\mu_{ij}^2)}{\rho_{ij}}, & \vec{v}_{ij} \cdot \vec{x}_{ij} < 0, \\ 0, & \vec{v}_{ij} \cdot \vec{x}_{ij} \geqslant 0 \end{cases} \tag{10}$$

with

$$\mu_{ij} = \frac{h_{ij}\vec{v}_{ij} \cdot \vec{x}_{ij}}{|x_{ij}|^2 + \eta^2}, \quad c_{ij} = \frac{1}{2}(c_i + c_j), \quad \rho_{ij} = \frac{1}{2}(\rho_i + \rho_j), \tag{11}$$

where c_i is the local sound speed and ρ_i is the local density at the ith particle. We also have

$$h_{ij} = 0.5(h_i + h_j), \quad \vec{x_{ij}} = \vec{x_i} - \vec{x_j} \quad \text{and} \quad \vec{v_{ij}} = \vec{v_i} - \vec{v_j} \tag{12}$$

with $\eta = 0.1\, h_{ij}^2$.

The AV is turned on only if particles are approaching each other, i.e., $\vec{v}_{ij} \cdot \vec{x}_{ij} < 0$. There are two parameters, α and β, whose values need to be chosen. These must, in general, be determined empirically. However,

there are, by now, fairly standard sets of α and β available in the literature. In this paper, we perform SPH simulations with two common (α, β) sets, viz., $(1, 2)$ and $(2.5, 2.5)$, hereafter referred to as SAV1 and SAV2, respectively.

2.1. Balsara switch

The Standard SPH viscosity SAV is prone to overestimating artificial viscosity, particularly in regions of strong shear, even when there is no compression [12,13]. Hence modifications have been suggested. In the present study, we have used Monaghan's AV scheme (MON) as well as Balsara's scheme (BAL).

In the BAL scheme [12], the factor μ_{ij} appearing in the standard viscosity expression is modified as follows:

$$\mu_{ij} = \frac{h_{ij}\vec{v}_{ij} \cdot \vec{x}_{ij}}{|r_{ij}|^2 + \eta^2}(f(i) + f(j)), \tag{13}$$

where

$$f(i) = \frac{|\langle \nabla \cdot v \rangle_i|}{|\langle \nabla \cdot v \rangle_i| + \langle \nabla \times v \rangle_i| + 0.0001 c_i/h}. \tag{14}$$

The function $f(i)$ is defined for each particle and carries information about the local flow [12]. It is devised to approach unity in regions of strong compression and zero in regions of strong vorticity. BAL is very commonly used in modern SPH codes. BAL, too, requires (α, β) to be set, and we have set these to $(1, 2)$.

2.2. Morris–Monaghan switch

The Morris and Monaghan modification (MON) [13] turns the parameters α,β into fields that evolve according to a simple source and decay equation. Like all fields, these fields are carried by SPH particles. The MON prescription is simplified by the arbitrary assumption $\beta = 2\alpha$. The source term causes α to grow as a particle enters a shock region, while the decay term causes α to decay behind the shock:

$$\frac{\mathrm{d}\alpha}{\mathrm{d}t} = -\frac{\alpha - \alpha^*}{\tau} + S. \tag{15}$$

The parameter α*, which is the value of the α field far from the shock, is set as 0.1 [13]. The relaxation timescale is given by $\tau = h/c$, where c is the speed of sound and h is the smoothing length. The source term is chosen to be $S = \max(-\nabla \cdot \boldsymbol{v}, 0)$. Other forms for S are possible and have been proposed [13].

2.3. Contact SPH

The contact SPH scheme (CON) is an attempt by Parshikov and co-workers [17,18] to improve SPH by eliminating arbitrary AV parameters. CON casts the problem of computing the derivative terms $\nabla\vec{v}, \nabla\sigma$ (stress tensor), that occur in the momentum and energy balance equations of SPH, into the solution of a Riemann problem [14]. The Riemann approach attempts to directly solve the conservation equations at the shock discontinuity and are commonplace for gas dynamic applications. However, the application of such methods to materials with strength has been rare, due to the increased complexity of formulation [21]. The solution of the Riemann problem yields the values of hydrodynamic fields at the contact surface. Note that in conventional SPH, the field values at the contact surface are just the mean values of the fields at interacting particles.

We have followed the formalism of [17], with one exception. In order to adapt CON to high-velocity impact, we have set the tangential components of the velocity, and the components of the stress tensor tangential to the

contact surface, equal to zero. This means that the terms entering the left part of Eqs. (25)–(28) of [17] have been eliminated. This reduces momentum transfer in the direction transverse to the impact direction.

The precise form of CON equations expressing conservation of momentum and energy employed in the present work is

$$\begin{aligned}\frac{\mathrm{d}\mathbf{v}_i}{\mathrm{d}t} &= -\sum_j \frac{2m_j\sigma^*_{ij}}{\rho_i\rho_j}\nabla W_{ij},\\ \frac{\mathrm{d}E_i}{\mathrm{d}t} &= \sum_j \frac{2m_j\sigma^*_{ij}(v_i^R - v^*_{ij})}{\rho_i\rho_j}\frac{\nabla W_{ij}\cdot(\mathbf{x}_i-\mathbf{x}_j)}{|\mathbf{x}_i-\mathbf{x}_j|},\end{aligned} \tag{16}$$

where

$$\sigma^*_{ij} = \frac{\sigma_j^R\rho_iC_i + \sigma_i^R\rho_jC_j + \rho_iC_i\rho_jC_j(v_j^R - v_i^R)}{\rho_iC_i\rho_jC_j},$$

and

$$v^*_{ij} = \frac{v_j^R\rho_jC_j + v_i^R\rho_iC_i - \sigma_j^R - \sigma_j^R}{\rho_iC_i\rho_jC_j},$$

with C_i, C_j being the sound speeds for particle i, j resp. and

$$\sigma_i^R = -p_i + (S_i^{xx}\delta x^2 + S_i^{yy}\delta y^2 + S_i^{zz}\delta z^2 + 2(S_i^{xy}\delta x\delta y + S_i^{yz}\delta y\delta z + S_i^{zx}\delta z\delta x))/(|\mathbf{x}_i-\mathbf{x}_j|^2),$$

with p_i being the pressure and S_i^{xx}, S_i^{xy}, etc. being components of the stress tensor for the ith particle. δx, δy, δz are the components of interparticle vector $x_i - \mathbf{x}_j$. Also

$$v_i^R = \frac{\mathbf{v}_i\cdot(\mathbf{x}_i-\mathbf{x}_j)}{|\mathbf{x}_i-\mathbf{x}_j|}.$$

And likewise for σ_j^R, v_j^R.

2.4. Validation of code

Our SPH code, with standard artificial viscosity SAV, has been validated in the simulations of spallation in metal plates [24]. The code with BAL and MON schemes developed out of this code, since BAL and MON are simply modifications of SAV. The Riemann code, employing the CON scheme, has been tested on simulations of a one-dimensional shock tube discussed in [18]. Another test of the SPH codes is whether or not they conserve energy and momentum, depending upon the imposed boundary conditions. With all AV options, the conservation equations are satisfied very well by our SPH codes.

3. Impact at a moderately high impact velocity

As our first test problem, we consider an impact problem studied by Howell and Ball [21]. This involves circular projectiles with a 1 cm diameter, made of Al or steel, impacting on 0.2 cm thick Al plates at a velocity of 3.1 km/s. In order to permit a comparison with the simulations of [21], our SPH simulations are done in 2D planar geometry and use a "stiffened gas" equation of state for both steel and Al, where the pressure p is given by

$$p = c_0^2(\rho-\rho_0) + (\gamma_0 - 1)\rho e,$$

where c_0 is the normal sound speed, ρ_0 is the normal density, e is the specific internal energy (energy per unit mass) and γ_0 is the Gruneisen parameter. An elastic–perfectly plastic constitutive model is used. The parameter values are those given in Table 1 of [21].

Particles are initially placed on a regular grid and the simulation is started at the moment of impact, with the particles in the projectile body being assigned the projectile velocity. The grid is rectangular, except that the circularity of the projectile is captured through two rings of equi-spaced particles along the circumference (Fig. 1). The particles are placed with an initial inter-particle distance of 0.01 cm. We thus have a total of 17,850 particles in the simulation, which includes 7820 in the projectile. The results are given below for $h/d = 1.4$ for all AVs, with the exception of CON, where $h/d = 1.7$ is used. This difference is because the CON scheme tends to have a slightly different range of stability, in terms of h/d, than other AVs – this is discussed in the next section.

Simulations are carried out for a total duration of 8 μs after impact. Three quantities are recorded, viz., the crater diameter, the post-impact longitudinal extension of the projectile, and the total longitudinal distance travelled by it in a given time-interval. Here, 'longitudinal' refers to the original direction of motion of the projectile. We also record the pressure at specified locations and times, as explained in the captions to Tables 1 and 2.

The upper halves of the target-projectile configurations, 8 μs after impact, are shown in Figs. 2 and 3 for Al–Al and steel–Al impacts, respectively.

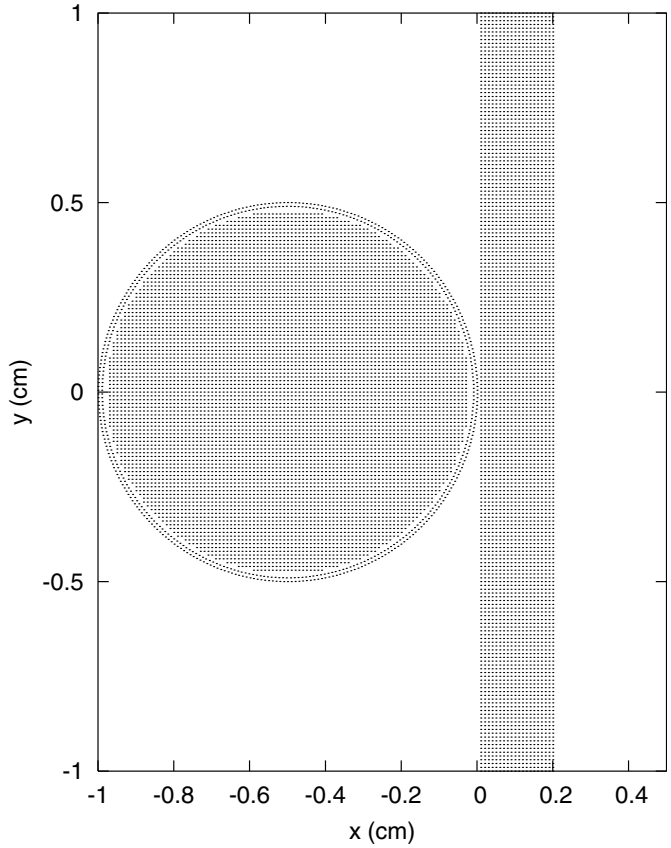

Fig. 1. Geometry and the initial particle placement for Al–Al impact. The initial condition is the same for different AV algorithms. The circular projectile, on the left, has a radius of 0.5 cm. On the right is the target plate having a thickness of 0.2 cm.

Table 1
Results for Al–Al impact at 3.1 km/s

Simulation	P_1 (GPa)[a]	P_2 (GPa)[b]	d_{cra} (cm)[c]	L_{extn} (cm)[d]	L_{proj} (cm)[e]
SAV1	18.0	−18.5	2.0	0.7	1.8
SAV2	17.5	−17.5	1.9	0.7	1.8
BAL	17.5	−18.5	2.0	0.7	1.8
MON	22.0	−13.5	2.0	0.8	2.0
CON	17.5	−14.0	2.1	0.7	1.9
HB[f]	18.6	−15.9	1.9	0.7	2.0

[a] Pressure generated at the center of the projectile 1 μs after impact.
[b] Peak tension generated in the projectile after the reflection of initial pressure wave, ~2.2 μs after impact.
[c] Crater diameter.
[d] L_{extn} = longitudinal extension of the projectile 8 μs after impact.
[e] Longitudinal distance travelled by the projectile in the 8 μs interval after impact. Pressures are calculated by summing over appropriate SPH particles. Lengths are resolved in SPH with a precision $\geqslant 2h$, and are quoted here to 0.1 cm.
[f] Results from the free lagrange simulation of Ball and Howell.

Table 2
Results for steel–Al impact at 3.1 km/s

Simulation	P_1 (GPa)[a]	P_2 (GPa)[b]	d_{cra} (cm)[c]	L_{proj} (cm)[d]
SAV1	27.0	−17.0	1.9	2.1
SAV2	25.0	−15.0	1.9	2.1
BAL	28.5	−10.0	1.8	2.2
MON	32.0	−9.5	1.8	2.2
CON	25.0	−10.0	1.7	2.2
HB[e]	27.9	−9.5	1.6	2.3

[a] Pressure generated at the center of the projectile 1 μs after impact.
[b] Peak tension generated at steel–Al interface due to reflection of the initial pressure wave from the rear end of the target.
[c] Crater diameter.
[d] Longitudinal distance travelled by the projectile in the 8 μs interval after impact. Pressures are calculated by summing over appropriate SPH particles. Lengths are resolved in SPH to $\geqslant 2h$, and are quoted here to 0.1 cm.
[e] The free lagrange simulation of Ball and Howell.

3.1. Results

The comparative plots of particle positions obtained by different AV schemes, Figs. 2 and 3, reveal interesting differences. All AVs, except for CON, show a tendency to yield clumps of particles. The absence of such clump formation and fracture from CON results is striking, especially when we note that no special method was employed to prevent tensile instability that is a cause of this phenomenon. BAL and MON appear to yield a greater extent of fracture than SAV1 and SAV2. Of all AVs considered here, the Riemann-based CON produces particle plots that are closest to the free lagrange Godunov method of [21]. Interestingly, Godunov methods are also Riemann-based.

The comparisons made with [21] are not absolute checks, in the sense that we are just comparing one numerical method with another, rather than with experimental results. Still, close agreement with published simulation results should give confidence in our results. Also, the differences yield interesting insights into the characteristics of SPH.

From Table 1 (Al–Al impact), we see that MON yields a substantially higher peak internal pressure in the projectile, P_1. We also note that MON has a disproportionately low value of the peak tension P_2. These two observations are consistent with evidence from Fig. 2 that the MON simulation suffers from large numerical fracture.

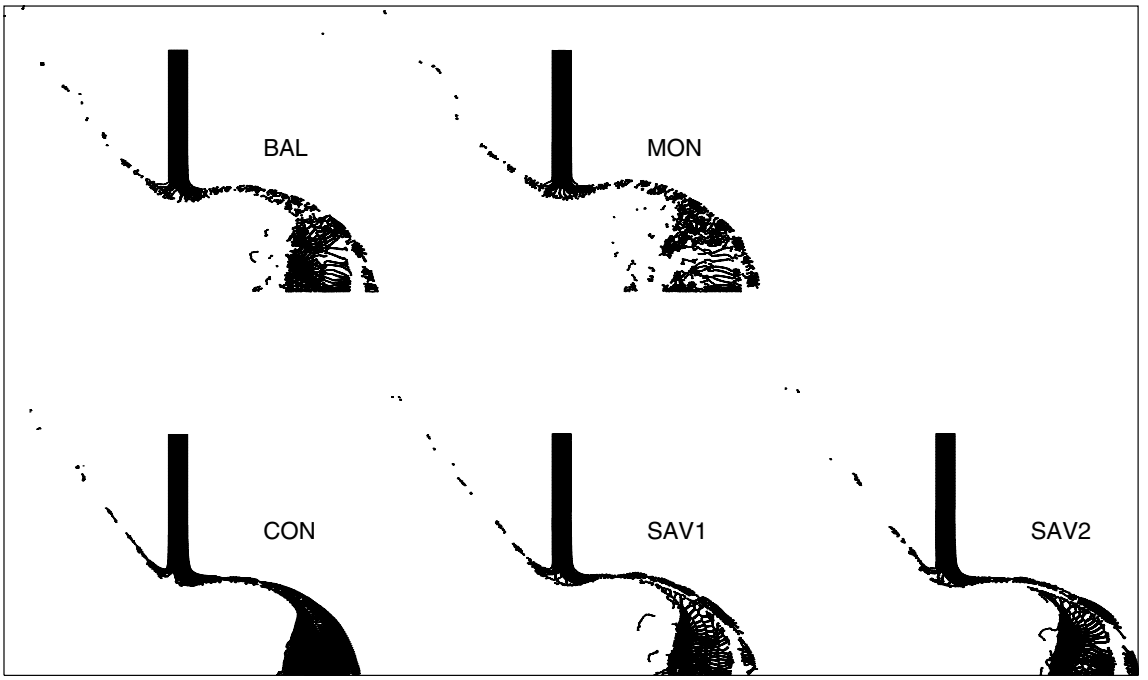

Fig. 2. Upper half of the configuration produced by Al–Al impact at a velocity of 3.1 km/s, at a time 8 μs after impact. Results are shown for different AVs.

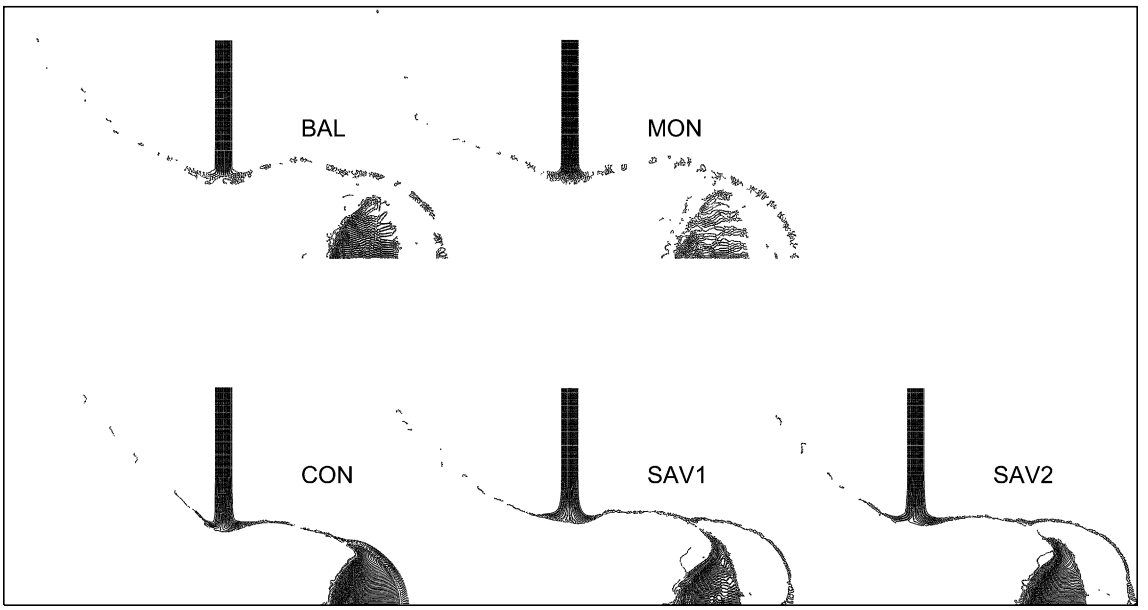

Fig. 3. Upper half of the configuration produced by steel–Al impact at a velocity of 3.1 km/s, at a time 8 μs after impact. Results are shown for different AVs.

Our simulations (both Al–Al and steel–Al) generally produce slightly larger crater diameters than those reported in [21] but slightly smaller L_{proj}. This indicates a potential AV problem: larger AV should, by increasing transverse momentum transfer, increase crater sizes. However, the relationship of AV to the longitudinal projectile momentum (as reflected in the distance travelled by the projectile in specified time) is not as clear-cut.

From Table 2 (steel–Al impact), we see that the MON simulation again yields the highest P_1. However, P_2 is quite uniform across MON, BAL, CON and HB simulations. The SAV1 and SAV2 simulations yield much higher values of P_2, along with a rather peculiar shape of the debris cloud.

Summarizing, impact simulations at 3.1 km/s using different AVs have shown that the CON method is least troubled with numerical fracture and the tendency to form clumps. Our SPH simulations agree among themselves on geometrical measurements of crater size, projectile extension and distance travelled by the projectile in a specified time. However, the projectile and debris cloud shapes differ as result of numerical fracture. Furthermore, the simulations show significant disagreement regarding the pressure which is monitored at two space–time locations. An inspection of Tables 1 and 2 shows that BAL and CON yield values for P_1 and P_2 that lie close to the mean of all AVs and also close to the mesh-based free lagrange simulation of [21].

We also find that the standard SPH AV (SAV) with common parameters performs as well as the modified AVs, BAL and MON, for Al–Al impact. However, in steel–Al impact, the performance of SAVs is markedly worse regarding the anomalously high value of the pressure P_2.

4. Hypervelocity impact

The work described in this section relates to the experiments done by Hiermaier et al. [23], in which aluminium spheres of 1 cm diameter are impacted onto thin aluminium or copper plates. The impact, at ~6 km/s, leads to the complete penetration of the target plate and the formation of a crater and debris cloud, whose dimensions after 20 μs evolution are compared with experimental data. Table 3 gives the necessary particulars (see also Fig. 1 of [23]). The simulations have been done in two and three spatial dimensions in cartesian coordinates. Data from three-dimensional (3D) simulations can be compared with experimental data in a straightforward manner. However, the heavy computational load necessitates the use of a smaller number of particles in each direction than that used in our 2D simulations. Hence, 3D simulations may not provide as detailed or accurate a picture of the impact process as the corresponding 2D simulations.

The simulations are run for 20 μs after impact. The ratio of the length to the width of the debris cloud at the end of a run yields the aspect ratio, which can then be compared with experimental values of the same [23]. The values for the post-impact longitudinal extension of the projectile or the longitudinal distance covered by the debris cloud are not experimentally provided.

In this study, a Mie-Gruneisen based six-parameter EOS [27] is used for copper and an HOM equation of state for aluminium [25]. Details are given in Appendix A. The Al–Al simulations are repeated with a Tillotson equation of state as well, parameters of which have been taken from [23]. The temperature and strain dependence of the shear modulus and yield strength are assumed to follow the Steinberg–Guinan model [26] (see Appendix A).

Table 3
The impact cases considered for hypervelocity impact (Section 4)

Projectile	Target	Projectile radius (cm)	Target thickness (cm)	Projectile velocity (km/s)
Al	Cu	0.5	0.15	5.75
Al	Al	0.5	0.40	6.18

4.1. 2D Simulation and results

The 2D simulations are done using 10,988 particles for Al–Al impact, including 2430 in the projectile, corresponding to an inter-particle spacing of 0.018 cm. The 2D Al–Cu impact has been modelled using 18,345 particles, including 7830 in the projectile, for an inter-particle spacing of 0.01 cm. In both cases, the impacting sphere is modelled as a cylinder with infinite length.

According to Balsara [12], SPH simulations are well-behaved only over a certain range of h/d. This range depends upon the particular problem and the precise form of the AV used. Simulations with unsuitable h/d values develop pathologies such as a rapid increase in the smoothing length. This, by increasing the number of neighbors over which summations must be done, quickly stalls the run. Some SPH methods vary the smoothing length by controlling the neighbor number, in which case the pathology takes a different form. We follow Benz's prescription for evolving the smoothing length [28]. In order to determine the useful range of h/d for different AVs, for the specific impact problem addressed here, we have repeated our simulations at h/d values ranging between 0.9 and 2.1.

The results on crater diameters and aspect ratio from SPH simulations, using techniques SAV1, SAV2, BAL, MON and CON, are presented in Tables 4 and 5. Note that the crater diameters are quoted to $\sim$0.05 cm – this follows from the fact that the resolution of an SPH simulation is approximately two smoothing lengths [12]. The crater diameter results are particularly interesting regarding the question of excessive numerical viscosity. An overly large numerical viscosity would transfer excessive momentum to

Table 4
Results for Al–Al impact at 6.18 km/s, obtained through 2D SPH simulations

Simulation	h/d range[a]	d_{cra} (cm)[b]	Aspect ratio[c]
SAV1	0.9–1.8	3.3	1.44
SAV2	0.9–1.4	3.2	1.40
BAL	1.0–1.8	3.3	1.37
MON	1.1–1.7	3.25	1.31
CON	1.4–2.0	3.25	1.44
EXP[d]		2.75	1.39

The results are given at $h/d = 1.4$ for SAV1, SAV2, BAL and MON and at $h/d = 1.7$ for CON.
[a] h/d range over which the SPH simulations, using the given AV, were stable for a duration of 20 μs.
[b] Crater diameter estimated with a precision of 0.05 cm.
[c] Aspect ratio of the debris cloud after 20 μs.
[d] Experimental data from Hiermaier et al.

Table 5
Results for Al–Cu impact at 5.75 km/s, obtained through 2D SPH simulations

Simulation	h/d range[a]	d_{cra} (cm)[b]	Aspect ratio[c]
SAV1	1.1–1.7	2.45	1.49
SAV2	1.1–1.6	2.45	1.40
BAL	1.2–1.8	2.45	1.50
MON	1.1–1.7	2.1	1.41
CON	1.3–2.1	2.5	1.51
EXP[d]		2.1	1.39

The results are given at $h/d = 1.4$ for SAV1, SAV2, BAL and MON, and at $h/d = 1.7$ for CON.
[a] h/d range over which the SPH simulations, using the given AV, were stable for 20 μs.
[b] Crater diameter estimated with a precision of 0.05 cm.
[c] Aspect ratio of the debris cloud after 20 μs.
[d] Experimental data from Hiermaier et al.

the transverse direction, yielding a crater diameter that is greater than the experimental value. That would also lead to an increase in the width of the cloud, implying a reduction in the aspect ratio. We indeed find that the numerical crater diameters are generally larger than the experimental values.

For Al–Al impact, the experimental data of Hiermaier et al. are provided in the form of two values for the crater diameter (Table II of [23]). The first value, $d_{cra} = 2.75$ cm, includes the crater lip, i.e., the mass hanging out of the crater, particularly on the downstream side. The second value, $d_{cra} = 3.45$ cm, excludes the lip. In our simulations, we define the crater diameter as the least distance between the crater lips, hence the lower value should be applicable. The computed values of d_{cra} are, however, well above this value and rather tend to approximate the mean of the two experimental values. The agreement between computational and experimental values is much better for the aspect ratio: for BAL the computed values lie within 2% of the experimental value over a wide h/d range. Other AV schemes achieve slightly less agreement – however, they still perform far better than those obtained by Hiermaier et al., whose numerical value of 1.11 for the Al–Al aspect ratio deviates by a much larger amount than in any of our simulations. The numerical aspect ratios are closely clustered around the experimental value.

However, it must be noted that the close agreement achieved by the numerical aspect ratios from different AVs obscures significant differences in the actual dimensions and shape of the debris cloud. MON and BAL produce debris clouds of similar shape (Fig. 4). The projectile gets completely shattered and fragmented, except in CON. Interestingly, the range of h/d for which SPH is stable is similar for SAV and the modified SAVs, as shown in Table 4. However, CON is only stable for somewhat larger value of h/d, implying that summation over more neighbors is required.

It is possible that differences between the assumed equation of state (EOS) and the true EOS could be the cause of mismatch between experimental and numerical crater diameters. Hence we repeated some of the simulations using the Tillotson EOS, with parameters listed in [23]. The Tillotson EOS incorporates the vapourization resulting from very high speed impact, hence it is relevant here. However, we do not find a significant change in the crater diameter, either quantitatively or qualitatively. Hence the EOS can be eliminated as a possible source of mismatch.

We next consider Al–Cu impact (Table 5, Fig. 5). We notice that the numerical d_{cra} for all methods, except MON, significantly diverge from the experimental d_{cra} value. During Al–Cu impact, the crater lips break away, hence the experimental crater diameter is reported as a single quantity. We find that MON is accurate over a large h/d range (1.1–1.7). Balsara's switch (BAL) turns out to be only as accurate as SAV1 and SAV2. The debris clouds produced through BAL and MON differ significantly as regards the distribution of projectile mass in the debris. The CON algorithm is only slightly less accurate as compared

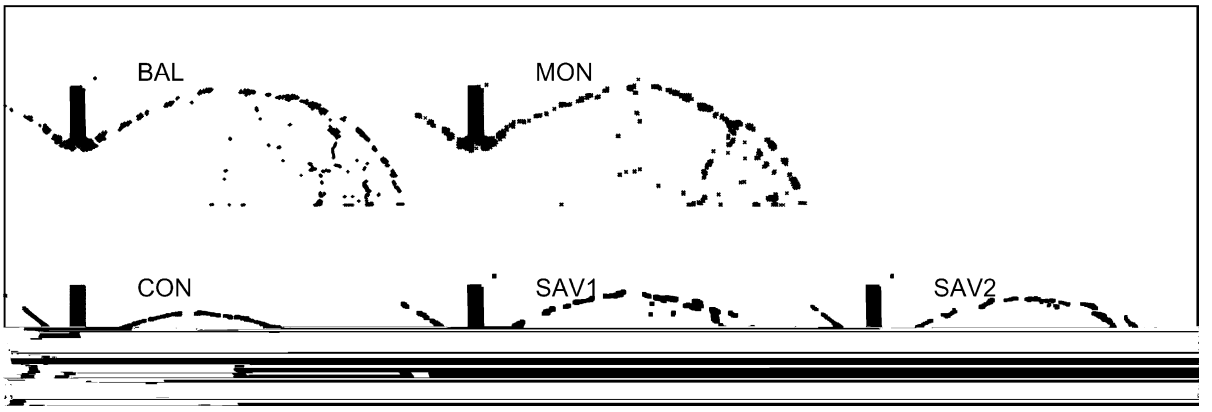

Fig. 4. SPH particle plots for 2D Al–Al hypervelocity impact obtained through different AVs after 20 μs evolution.

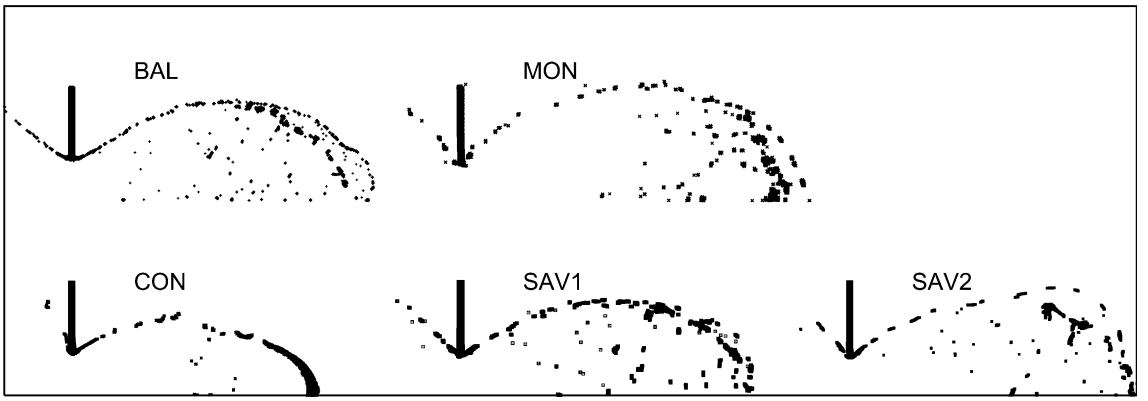

Fig. 5. SPH particle plots for 2D Al–Cu hypervelocity impact obtained through different AVs after 20 μs evolution.

to SAVs and BAL in terms of both the crater diameter and the aspect ratio. CON retains the pattern of requiring larger h/d values than other AVs, as shown in Table 5.

4.2. 3D Simulation and results

The 2D simulations described above assume that the projectile is an infinitely long cylinder. Now, the actual experiments involved a spherical projectile. Hence, for a definitive comparison, we must perform a set of 3D simulations. These simulations are done at a single h/d value. Based on the results of Section 4.1, we choose $h/d = 1.4$ for all AVs except CON, which is done at $h/d = 1.7$.

The results obtained through 3D simulations with different AVs are given in Tables 6 and 7 for Al–Al and Al–Cu impact, respectively. For Al–Al impact, a total of 2.36×10^5 particles, including 1.1×10^4 in the projectile, were employed. Even with this large number of particles, all the AVs tend to overestimate the aspect ratio. From Table 6, we find that CON is closest to the experimental d_{cra}, the SAVs underestimate it, while BAL and MON still overestimate d_{cra}. Some further insight can be obtained by examining the particle plots in Fig. 8. CON, while providing a close match with d_{cra}, does not reproduce the experimental debris cloud very well. In particular, we see that the backward-moving component of the debris cloud is very weak in CON. Here, 'backward-moving' refers to the debris fragments that are moving in a direction opposite to the impact direction. The cloud is overcompressed in CON and SAV2.

Table 6
Results for Al–Al impact at 6.18 km/s, obtained through 3D SPH

Simulation	d_{cra} (cm)[a]	Aspect ratio[b]
SAV1	2.5	1.74
SAV2	2.4	1.90
BAL	3.1	1.53
MON	3.2	1.53
CON	2.75	1.67
EXP	2.75	1.39

EXP refers to the experiment of Hiermaier et al.

[a] Crater diameter.

[b] Aspect ratio of the debris cloud after 20 μs evolution. All lengths are estimated with a precision of 0.05 cm. All simulations have been done at $h/d = 1.4$, except for CON, which has been done at $h/d = 1.7$.

Table 7
Results from Al–Cu impact at 5.75 km/s, obtained through 3D SPH

Simulation	d_{cra} (cm)[a]	Aspect ratio[b]
SAV1	2.3	1.9
SAV2	2.2	1.75
BAL	2.2	1.7
MON	2.25	1.85
CON	2.0	2.3
EXP	2.1	1.39

EXP refers to the experiment of Hiermaier et al.
[a] Crater diameter.
[b] Aspect ratio of the debris cloud after 20 μs evolution. All lengths are estimated with a precision of 0.05 cm. All simulations have been done at $h/d = 1.4$, except for CON, which has been done at $h/d = 1.7$.

It is possible that the mismatch may be due to the use of an inadequate number of particles. Hence we have repeated the runs with different numbers of particles. The convergence of the results is illustrated in Figs. 6 and 7 for Al–Al impact. In these figures, d_{cra} and aspect ratio are plotted against N_{acr}, the number of particles initially placed across the target. The initial inter-particle spacing, given by d (cm) $= 0.4/(N_{acr}-1)$, thus varies from 0.08 to 0.036 cm, corresponding to a factor of 10 increase in the number of particles. Over this range, d_{cra} and aspect ratio computed using BAL and MON show little change. Thus BAL and MON display a fairly reasonable degree of convergence while SAV1 and CON show overall poorer convergence. However, for MON and BAL, the final value of d_{cra}, at the largest N_{acr}, is still significantly higher than the experimental value, indicating either that the problem with excess AV persists in 3D, or else the problem lies with the equation of state or the material strength model. Now, our experience with changing the EOS model in 2D simulations indicates that EOS is not likely to be responsible. Hence either the material strength model, or excess AV, is a major problem during hypervelocity impact.

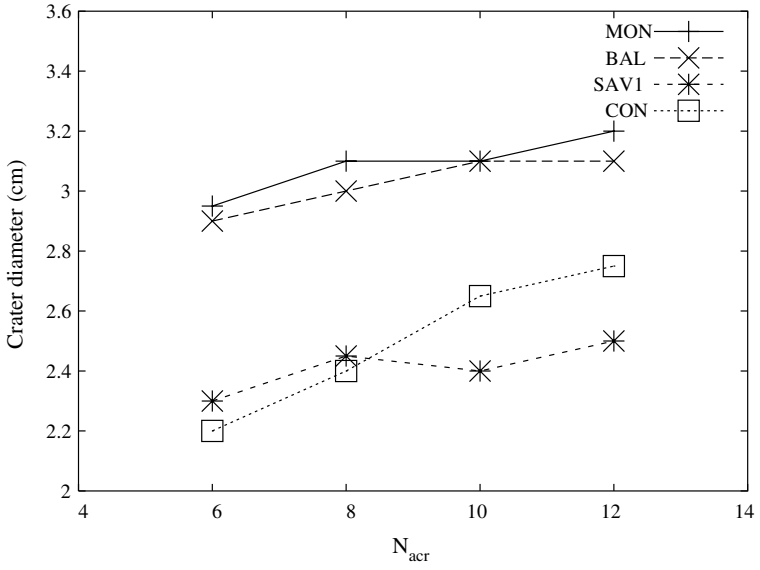

Fig. 6. Convergence in 3D Al–Al hypervelocity impact SPH simulations with different AVs. Curves show d_{cra} as a function of N_{acr}, the number of SPH particles initially placed across the target plate.

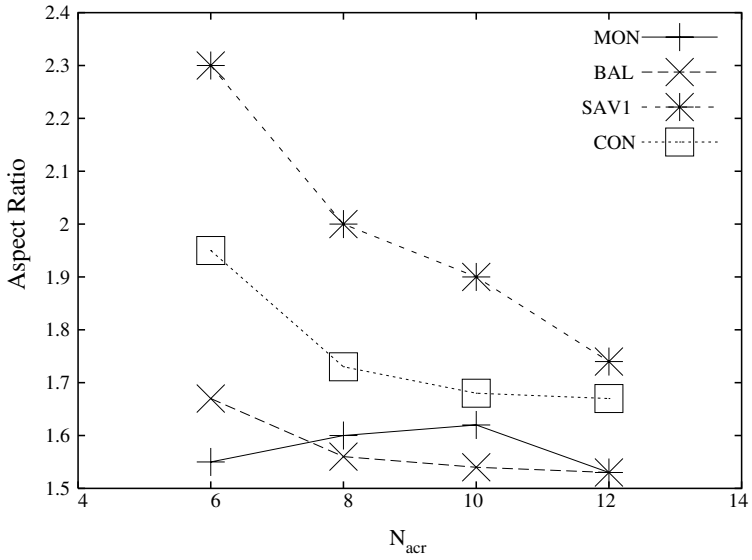

Fig. 7. Convergence in 3D Al–Al hypervelocity impact SPH simulations with different AVs. Curves show aspect ratio as a function of N_{acr}, the number of SPH particles initially placed across the target plate.

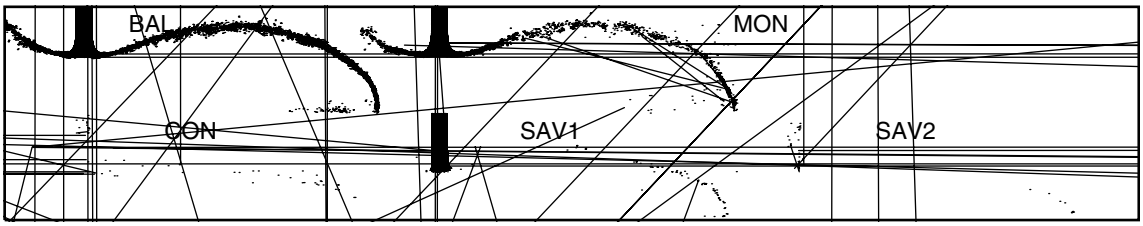

Some of the above simulations of Al–Al impact have been repeated using Monaghan's XSPH prescription [29], as modified by Balsara [12] for position update:

$$\mathbf{v}_{i,\mathrm{update}} = \mathbf{v}_i + 0.1\left(\sum_j \frac{2m_j}{(\rho_i + \rho_j)}(\mathbf{v}_i - \mathbf{v}_j)W_{ij}\right),$$

where $\mathbf{v}_{i,\mathrm{update}}$ is the velocity of the ith particle by which the spatial coordinates of a SPH particles are updated:

$$\mathbf{x}_i^{n+1} = \mathbf{x}_i^n + \mathrm{d}t\,\mathbf{v}_{i,\mathrm{update}}.$$

However, even this change did not improve the agreement of d_{cra} and aspect ratios with experimental values.

Al–Cu impact at 5.75 km/s has also been simulated in 3D, with an inter-particle spacing of 0.03 cm (see Fig. 9). The total number of particles is now $\sim 1.25 \times 10^5$, including $\sim 1.9 \times 10^4$ in the projectile. We find closer agreement with experimental data in terms of d_{cra} as compared with 2D Al–Cu impact simulations. However, the aspect ratios reveal problems with this set of simulations. The aspect ratios are significantly larger than experimental values, the closest match coming from BAL, which is still 22% higher than in experiment. CON overestimates the aspect ratio by a particularly large margin while slightly underestimating d_{cra}. Taken

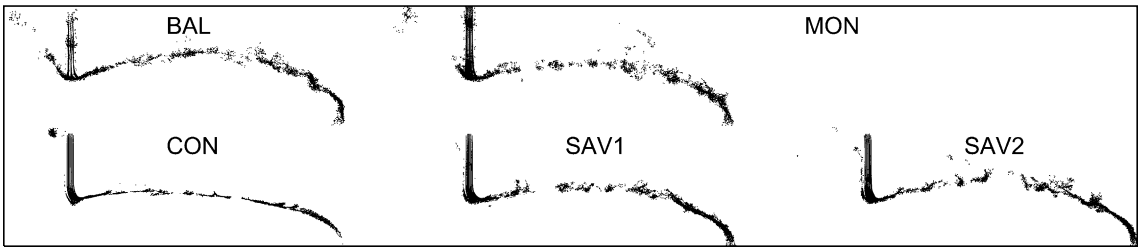

Fig. 9. SPH particle plots for 3D Al–Cu hypervelocity impact obtained through different AVs after 20 μs evolution. Every fifth particle is plotted.

together with $d_{cra} = 2.75$ cm for 3D CON Al–Al impact, this raises an intriguing point: whether the 3D CON simulations are suffering from an overcompensation of excess AV and thus the deleted tangential wave terms should be reinserted (cf. Section 2.3). However, this possibility is not explored in this work.

This wider discrepancy, relative to 3D Al–Al impact, could be due to an insufficient number of SPH particles, i.e., a lack of resolution. It appears that more resolution is required when we have SPH particles with differing masses – if both Al and Cu particles are equally sized, there exists a mass discrepancy of 3.2 times between two species of SPH particles. A similar effect was found in our 2D hypervelocity simulations, where larger numbers of particles were required to sufficiently resolve Al–Cu impact as compared to Al–Al impact. This phenomenon has not yet received sufficient attention in the literature. However, [30] has given some indication of the problems that occur due to large mass difference between SPH particles.

For 3D Al–Cu impact, best overall agreement is obtained through BAL and SAV2 and MON to a lesser extent. It was found necessary to stabilize MON by imposing a lower limit of α^* on the field variable α (Eq. 15). It appears that the very close match found in 2D MON for Al–Cu crater size was fortuitous, since it is not repeated in 3D. The CON scheme was unable to resolve Al–Cu impact satisfactorily, producing a highly overcompressed debris cloud.

4.3. Summary of results for hypervelocity impact

Simulations have first been done in two spatial dimensions. These have yielded the useful range of h/d values for different AV schemes. Next, since planar simulations imply a geometry very different from that in the experiment, the simulations are repeated in 3D, with two interesting results. Firstly, we find that convergence of results with the number of simulation particles is rather slow for some schemes. Secondly, looking at the schemes that have converged, we find that BAL and MON are the most suitable for hypervelocity impact. But even these overestimate the crater diameter by 12–16% in Al–Al impact. Experimental agreement is generally worse for Al–Cu impact. The SAV schemes, as well as CON, do not obtain the correct debris cloud shape as measured through the aspect ratio.

We also conclude that, given the present restrictions on our computational resources, we are not able to resolve the impact event sufficiently in 3D simulations as to be an improvement over 2D simulations. The use of greater resources should permit a better match with experiment. We plan to parallelize the SPH code to make use of a PC cluster.

5. Conclusions

Two distinct problems, involving high-velocity impact and penetration of metallic projectiles through thin metallic plates, have been simulated through four different SPH methods. The SPH methods differ in their artificial viscosity (AV) schemes.

We first apply these AVs to a case of moderately high velocity impact. These simulations have been done in 2D planar geometry and use an elastic–perfectly plastic constitutive model. This is done in order to compare with the free lagrange simulations of [21]. Comparison is made through quantities like the crater diameter, the distance travelled by the projectile in a specified time interval after impact, and values of the pressure at specified positions and times. The CON scheme gives the best overall results. In particular, it does not suffer from numerical fracture and 'clump formation' that are very visible in SAV and modified SAV (MON and BAL) simulations. Differences are slight between different AVs regarding geometrical quantities, but are greater when specified pressures are compared. This comparison leads us to have more confidence in CON and BAL, and to a lesser degree in MON. The standard SPH viscosity SAV does not fare well, particularly for steel–Al impact. The general agreement with published results gives us confidence in our study.

We have next compared the performance of these schemes on hypervelocity impact experiments performed by Hiermaier et al. [23]. The projectile is completely shattered and a debris cloud forms and moves onward. These simulations use the Steinberg–Guinan material strength model. Simulations have first been done in two spatial dimensions. These have yielded the useful range of h/d values for different schemes. Next, since planar simulations imply a geometry very different from that in the experiment, the simulations are repeated in 3D, with two interesting results. Firstly, we find that convergence of results with the number of simulation particles is rather slow for some schemes. Secondly, looking at the schemes which have converged, we find that BAL and MON are the most suitable for hypervelocity impact. But even these overestimate the crater diameter by 12–16% in Al–Al impact. The SAV schemes, as well as CON, do not obtain the correct debris cloud shape as measured through the aspect ratio.

The overestimation of the crater size in hypervelocity impact could be attributed to excess AV, which enhances transverse momentum transfer. We have also found that the choice of alternative equations of state does not significantly change the results.

The CON algorithm, with its attractive quality of being free from arbitrary parameters, is promising. At moderate impact velocities, it performs as well as more conventional SPH methods, while not suffering from numerical fracture that plagues other SPH methods. However, it does not perform as well in the hypervelocity impact regime. However, CON relies upon a low-order approximation of the Riemann problem, and a better approximation such as Dukowicz's iterationless solution should help improve CON.

It is clear that better control, including better diagonstics, would be very helpful in resolving the question of artificial viscosity for SPH techniques. Use of newer techniques such as tensor viscosity [8] could be useful, though at a greater computational cost.

Acknowledgements

We thank V.R. Ikkurthi, A. Majalee and S. Madhavan for providing modules that implement equations of state and constitutive models used in this work. V.R. Ikkurthi is further thanked for discussions.

Appendix A

The equations of state and material models used in Section 4 are briefly discussed in this appendix.

A.1. Six-parameter equation of state

A six-parameter equation described in [27] has been used for copper. The pressure is computed as

$$P = P_{\text{cold}} + P_{\text{th}},$$

where P_{cold} is the cold contribution to the pressure and is a function of reduced density $\eta = \rho/\rho_0$:

$$P_{\text{cold}} = \sum_{i=1}^{6} a_i \eta^{i/3+1}.$$

The coefficients a_i are obtained by imposing six constraints. Details may be obtained from [31].

The thermal contribution to the pressure is

$$P_{\text{th}} = \rho_0 \gamma (U - U_{\text{cold}}),$$

with γ being Gruneisen's constant and U_{cold}, the cold contribution to specific energy:

$$U_{\text{cold}} = \frac{3}{\rho_0} \sum_{i=1}^{6} \frac{a_i}{i} (\eta^{i/3} - 1).$$

A.2. HOM equation of state

The HOM equation of state [25] has been used for aluminium for simulations described in Section 3. Some details are given below.

A.2.1. Compression: $\rho > \rho_0$

Here, the pressure P is

$$P = P_{\text{h}} + \rho \gamma (U - U_{\text{h}}),$$

with ρ, U being the current density and specific energy resp. ρ_0 is the reference density and γ is the Grunenisen constant. P_{h} is the pressure on hugoniot, provided by the Rankine–Hugoniot relation (in terms of specific volumes, $V_0 = 1/\rho_0$ and $V = 1/\rho$.)

$$P_{\text{h}} = \frac{C^2 (V_0 - V)}{[V_0 - S(V_0 - V)^2]},$$

C and S are material-dependent constants. The specific energy on the hugoniot is

$$U_{\text{h}} = \frac{P_{\text{h}} (V_0 - V)}{2}.$$

A.2.2. Rarefaction: $\rho < \rho_0$

In this case we have,

$$P = \left[U - \frac{C_{\text{v}}}{3\alpha} \left(\frac{\rho_0}{\rho} - 1 \right) \right] \gamma \rho,$$

with C_{v} the specific heat and α being the coefficient of linear expansion.

A.3. Steinberg–Guinan model

The Steinberg–Guinan strain-rate independent model describes the dynamic yield strength and shear modulus as functions of pressure, temperature and plastic strain:

$$Y = [Y^0 (1 + \beta \epsilon^{\text{P}})^n][1 + bPV^{1/3} - h(T - 300)],$$

where ϵ^{P} is the equivalent plastic strain and $V = 1/\rho$, with the conditions

$$\begin{aligned} &Y^0(1+\beta\epsilon^{\mathrm{P}})^n \leqslant Y_{\max}, \\ &Y = 0 \quad \text{for } T > T_{\mathrm{m}}, \quad T_{\mathrm{m}} = T_{mo}V^{2/3}\exp[2\gamma(1-V)]. \end{aligned} \tag{17}$$

The shear modulus variation is given as

$$\mu = \mu_0[1 + bPV^{1/3} - h(T - 300)].$$

Here, Y_0, $Y_{\max}$, β, h, n, T_{mo} and γ are material constants. T_{m} is the density-dependent melting point.

References

[1] L.B. Lucy, Astronom. J. 83 (1977) 1013.
[2] R.A. Gingold, J.J. Monaghan, Mon. Not. R. Astronom. Soc. 181 (1977) 375.
[3] G.R. Johnson, E.H. Petersen, R.A. Stryk, Incorporation of an SPH option into the EPIC code for a wide range of high velocity impact computations, Int. J. Impact Eng. 14 (1993) 385.
[4] M.B. Liu, G.R. Liu, Z. Zong, K.Y. Lam, Computer simulation of high explosive explosion using smoothed particle hydrodynamics methodology, Comput. Fluids 32 (2003) 305.
[5] Myers, Dynamic Behavior of Materials, Wiley, New York, 1994.
[6] J. Campbell, R. Vignjevic, L. Libersky, A contact algorithm for smoothed particle hydrodynamics, Comput. Methods Appl. Mech. Eng. 184 (2000) 49.
[7] K. Shintate, H. Sekine, Composites A 35 (2004) 683.
[8] J. Owen, The tensor artificial viscosity for SPH, Comput. Phys. (2004).
[9] K. Jach, J. Leliwa-Kopystynski, M. Mroczkowski, et al., Free particle modelling of hypervelocity asteroid collisions with the Earth, Planetary Space Sci. 42 (1994) 1123.
[10] P.W. Randles, L.D. Libersky, Smoothed particle hydrodynamics: some recent improvements and applications, Comput. Meth. Appl. Eng. 139 (1996) 375.
[11] A.K. Chaniotis et al., Remeshed smoothed particle hydrodynamics for the simulation of laminar chemically reactive flows, J. Comput. Phys. 191 (2003) 1.
[12] D.S. Balsara, von Neumann stability analysis of smoothed particle hydrodynamics – suggestions for optimal algorithms, J. Comput. Phys. 121 (1995) 357.
[13] J.P. Morris, J.J. Monaghan, A switch to reduce SPH viscosity, J. Comput. Phys. 136 (1997) 41.
[14] J. Dukowicz, A general, non-iterative Riemann solver for Godunov's method, J. Comput. Phys. 61 (1985) 119.
[15] J.J. Monaghan, SPH and Riemann solvers, J. Comput. Phys. 136 (1997) 298.
[16] S. Inutsuka, Reformulation of smoothed particle hydrodynamics with Riemann solver, J. Comput. Phys. 179 (2002) 238.
[17] A. Parshikov, S.A. Medin, Smoothed particle hydrodynamics using interparticle contact algorithms, J. Comput. Phys. 180 (2002) 358.
[18] A. Parshikov, S.A. Medin, I. Loukashenko, V. Milekhin, Improvements in SPH method by means of inter-particle contact algorithm and analysis of perforation tests at moderate projectile velocities, Int. J. Impact Eng. 24 (2000) 779.
[19] G.R. Johnson, R.A. Stryk, S.R. Beissel, SPH for high velocity impact computations, Comput. Meth. Appl. Mech. Eng. 139 (1996) 347.
[20] J.C. Lombardi Jr., A. Sills, F.A. Rasio, S.L. Shapiro, Tests of spurious transport in smoothed particle hydrodynamics, J. Comput. Phys. 152 (1999) 687.
[21] B.P. Howell, G.J. Ball, A free-lagrange augmented Godunov method for the simulation of elasticplastic solids, J. Comput. Phys. 175 (2002) 128.
[22] J. Hongbin, D. Xin, On criterions for smoothed particle hydrodynamics kernels in stable field, J. Comput. Phys. 202 (2005) 699.
[23] S. Hiermaier, D. Konke, A.J. Stilp, K. Thoma, Computational simulation of the hypervelocity impact of Al-spheres on thin plates of different materials, Int. J. Impact Eng. 20 (1997) 363.
[24] V. Mehra, V.R. Ikkurthi, S. Chaturvedi, Spalling in impacted metal plates: a study using smooth particle hydrodynamics simulationsProceedings of the 21st International Symposium on Ballistics, Defence Science and Technology Organisation, 2004.
[25] C. Mader, Numerical Modelling of Detonations, University of California Press, 1979.
[26] M.L. Wilkins, Computer Simulation of Dynamic Phenomena, Springer, Berlin, 1999.
[27] S. Elizer, A. Ghatak, H. Hora, E. Teller, An Introduction to Equations of State: Theory and Applications, Cambridge University Press, Cambridge, 1986.

[28] W. Benz, Applications of smooth particle hydrodynamics to astrophysical problems, Comput. Phys. Commun. 48 (1988) 97.
[29] J.J. Monaghan, On the problem of penetration in particle methods, J. Comput. Phys. 82 (1989) 1.
[30] S.J. Schraml, K.D. Kimsey, Smoothed particle hydrodynamics simulation of disk-shaped penetrator impact, DTIC Report ARL-TR-1766, August, 1998.
[31] V.R. Ikkurthi, S. Chaturvedi, Use of different spallation models for simulating impact-driven spallation in metal plates, Int. J. Impact Eng. 30 (2004) 275.